Attrition of Ca-Based CO_2-Adsorbents by a High Velocity Gas Jet

Jose Manuel Valverde and Miguel Angel Sanchez Quintanilla
Dept. of Electronics and Electromagnetism, Faculty of Physics, University of Seville, Avenida Reina Mercedes s/n,
41012 Sevilla, Spain

DOI 10.1002/aic.13908

Attrition of Ca-based adsorbents is a subject of interest that determines the efficiency of the Ca-looping process for CO_2 capture. In this article, we report an experimental test to assess the mechanical strength of cohesive Ca-based adsorbents based on particle sizing by laser diffractometry. In this technique, the powder sample is dispersed, either by a high velocity air jet (dry dispersion) or by a liquid before the particle size distribution (PSD) is measured. In the dry dispersion unit, particle aggregates are subjected to high energy collisions intended to cause their fragmentation. The PSDs obtained at a low dispersive air pressure for calcined CaO shows that there is a remarkable population of large aggregates due to strong van der Waals of attraction. A second population consists of compact small aggregates, which are relatively stronger due to material sintering at interparticle contacts. As the dispersive air pressure is increased, these aggregates are broken. Their size scales as a power law of the jet air velocity in agreement with the prediction of a fracture mechanics theory of brittle materials. In contrast, the population of large aggregates of a modified adsorbent, consisting of a CaO/nano-silica composite, is not significative, which can be attributed to the effect of nano-silica in decreasing the van der Waals attractive force. Moreover, the small compact aggregates of the composite are broken at a lower rate with the dispersive air pressure. The enhanced strength of these composite aggregates is further supported by the PSDs obtained for samples dispersed in a liquid and previously excited by high energy ultrasonication. © 2012 American Institute of Chemical Engineers *AIChE J*, 59: 1096–1107, 2013

Keywords: powder technology, particulate processes, Attrition, Ca-based adsorbents, granular materials, powders

Introduction

The study of CO_2 adsorbents based on CaO powders has become a topic of increasing interest in the recent years due to their potential use in industry for efficient capture of CO_2 by means of the Ca-looping process.[1] The Ca-looping process is realized by means of two interconnected circulating fluidized beds. The Ca-based adsorbent reacts in the fluidized bed carbonator with the CO_2 to form $CaCO_3$ (limestone) at temperatures around 650°C. The spent adsorbent is then regenerated by calcining it at high temperatures (typically between 850 and 1100°C) in a second fluidized bed reactor (calciner) interconnected with the carbonator. In the calciner, $CaCO_3$ decomposes to yield CaO and a pure stream of CO_2 ready to be compressed and transported for sequestration. Another technology that might benefit from the Ca-looping process is steam methane reforming to produce hydrogen from natural gas. In the so-called sorption enhanced steam methane reforming (SE-SMR) process, higher methane to hydrogen conversion and improved energy efficiency are achieved by on-line capture of CO_2 while steam methane reforming and water gas shift reactions take place.[2]

The CO_2 capture capacity of Ca-based adsorbents decreases with increasing the number of calcination–carbonation cycles, which is mainly attributed to the decrease of the reactive surface area as a result of material sintering during calcination.[1,3] A large amount of the current research on this issue is thus aimed at the development of modified adsorbents with improved long-term capture performance.[1] A further common drawback that affects the performance of the Ca-looping process is particle size reduction due to attrition and particle shrinkage.[1,4] Experimental results show that attrition of limestones in fluidized beds depends on particle properties, bed temperature, heating rate, calcination time, and fluidizing gas velocity.[5–7] As a common feature, particle size distribution (PSD) analyses of limestones used in Ca-looping pilot-scale tests indicate a high attrition rate during first calcination.[1,8,9] Upon subsequent cycling, the attrition rate is reduced, but the continuous decrease of particle size still poses a problem for the scaling-up of the Ca-looping process.[1] Some natural limestones used in a pilot-scale Ca-Looping process were found to be particularly fragile during the initial calcination and the first few hours of circulation, showing a particle size reduction by a factor of around two.[8] The low strength exhibited by calcined limestone has also been reported by Scala et al.[6] from experiments in which the samples were subjected to collisions against a target by high velocity air jets. Thus, not just the thermal stability of newly

---

Correspondence concerning this article should be addressed to J. M. Valverde at jmillan@us.es.

developed synthetic adsorbents, but also their mechanical stability, should be a key subject of research.[1] Even though there are few studies addressing the resistance to attrition of synthetic adsorbents, it seems clear that the use of additives or alteration of the material morphology has a significant effect on their mechanical strength. Manovic and Anthony[10] observed that synthetic adsorbents consisting of pellets prepared using $Ca(OH)_2$ and calcium aluminate cement lost strength after many carbonation/calcination cycles, and they attributed it to the development of cracks. Pacciani et al.[11] showed that synthetic adsorbents containing mayenite suffered a lower degree of attrition than those supported on MgO, which was attributed to the reaction occurring between Al_2O_3 and CaO during the formation of mayenite.

In general, an important cause of attrition in industrial processes involving fluidization is the so-called secondary fragmentation due to collisions against targets. This mainly takes place in the jetting region of the fluidized bed and in the exit region of the riser and the cyclone of circulating fluidized bed reactors.[6,12] Single particle impact attrition tests show that the impact attrition rate R and the impact velocity v are related by the power law $R \propto v^k$, where the so-called impact attrition index k is around $k = 2$ for crystalline materials and depends on internal and surface defects and particle structure.[13] In the experimental work reported by Scala et al.[6] on impact fragmentation of calcined limestone, the attrition rate was shown to follow this power law, with $k \simeq 1.3$ throughout a range of impact velocities between 10 and 80 m/s. In fluidized beds used in industry applications, attrition is mainly produced by the impact breakage of particles entrained into the air jets ejected from perforated orifices at the gas distributor plates.[13] Particle velocities v_p in the jet are smaller than the orifice gas velocity v_g (v_p rarely exceeds 10 m/s, while v_g can be larger than 60 m/s[13]). By coupling a hydrodynamic model, which was useful to compute the particle velocities as a function of the orifice gas velocity, to single particle attrition tests,[13] Ghadiri et al.[13] arrived also at a power-law dependence of the attrition rate on orifice gas velocity $R \propto v_g^{\delta}$. According to experimental data reviewed by Boerefijn et al.,[14] the attrition rate caused by air jets in fluidized beds of catalyst particles in a range of gas velocities between 50 and 300 m/s could be well fitted by this power law, with δ increasing from 1.5 to 2.9 as particle size was increased from 75–90 μm to 106–125 μm.

In the experimental work reported in the present article, the PSDs of predispersed Ca-based adsorbents are measured by laser-difractometry. Dispersion is performed by subjecting the powder to a high-velocity air jet. The evolution of the PSD as the dispersive air pressure is increased gives an idea of the possible attrition of particles as due to mechanical collisions generated in the dispersion unit. This method has been recently proposed[15,16] to quantify particles' attrition in the pharmaceutical industry instead of the standard time-consuming granule breaking strength test. The experimental results reported in this paper indicate that the use of nanosilica as additive serves to enhance the resistance to attrition of calcined CaO.

Materials and methods

The Ca-based adsorbent used is a commercial $Ca(OH)_2$ powder (Merck). Primary particle size in this powder is in the range of microns as seen in SEM images (Figure 1a), particle density (determined by an AccuPyc 1330 Pycnometer) is 2.36 g/cm^3, and the BET surface area is 16.3 m^2/g (measured by N_2 physisorption analysis). Because of the prevalence of attractive van de Waals forces between primary particles over their weight, these particles join into agglomerates of size between tens and hundreds of microns. A modified adsorbent (presented in Ref. 17) was prepared by a physical dry mixture of $Ca(OH)_2$ with a nanostructured silica powder (Aerosil®R974 from Degussa). Primary silica nanoparticles of this powder aggregate during the flame synthesis process at high temperatures, forming fractal aggregates wherein nanoparticles are permanently held together by strong chemical bonds because of material sintering[18] (see Figure 1b). Nano-silica aggregates form highly porous agglomerates due to attractive van der Waals forces of size on the order of tens of microns (see Figure 1c).[19]

The use of nanopowders as flow conditioners of fine cohesive powders is well documented in the literature.[20] The interparticle attractive force between fine particles whose surface has been uniformly coated with hard nanoparticles such as silica nanoparticles is decreased, which improves the powder flowability and fluidizability. To this end, the mixing method has to be sufficiently effective to achieve a uniform surface coating. Dry coating techniques such as magnetic assisted impaction coating and ball milling are useful to improve the dispersion of silica nanoparticles onto the host particles of the fine cohesive powder. Using these techniques, the nanoparticle agglomerates are disrupted down to a submicrometer scale, and the powder particles are coated during collisions, yielding a uniform nanoparticle coating of the host particles.[20] Besides decreasing cohesiveness, nanoparticle coating can be useful to increase the mechanical strength of the composite material.[21] In our study, we have chosen the simplest process to mix the $Ca(OH)_2$ powder with the silica nanopowder, just consisting of dry physical mixing by hand. Our motivation to use this simple process was to keep the costs and technical difficulties associated with preparation of the modified adsorbent as low as possible.

After dry physical mixing, the silica nanoparticle agglomerates that remain unbroken are seen to be coated by small $Ca(OH)_2$ aggregates (Figure 1d), which can be attributed to contact charging. When two insulators with different dielectric constants are in contact, it is energetically favorable that the one with the higher dielectric constant donates electrons to the other, as can be seen from the correlation between the order of materials in the triboelectric series and their dielectric constant.[22] The relative dielectric constant of $Ca(OH)_2$ is 11.8, while that of SiO_2 is around 4.4.[23] It is therefore likely that strong electrostatic forces of attraction are established at the contact between nano-silica and $Ca(OH)_2$ since both materials are placed at the distant extremes of the triboelectric series.[22]

The light silica nanoparticle agglomerates, which fluidize easily, play the role of carriers of the cohesive $Ca(OH)_2$ particles, providing them with a vehicle for improved fluidization. Since the $Ca(OH)_2$ aggregates become better dispersed and the fluidizability of the composite is enhanced, the CO_2 adsorption performance in a fluidized bed is improved as shown in Refs. 17 and 24. Thermo-gravimetric tests, at conditions close to the Ca-Looping process, have shown also that carbonation in the fast stage is accelerated for the composite adsorbent due to the increase of the effective contact surface between CO_2 and the adsorbent, and the residual capture capacity is increased because of enhanced thermal stability.[25] In this work, the mechanical strength of calcined samples of the original adsorbent ($Ca(OH)_2$) and the

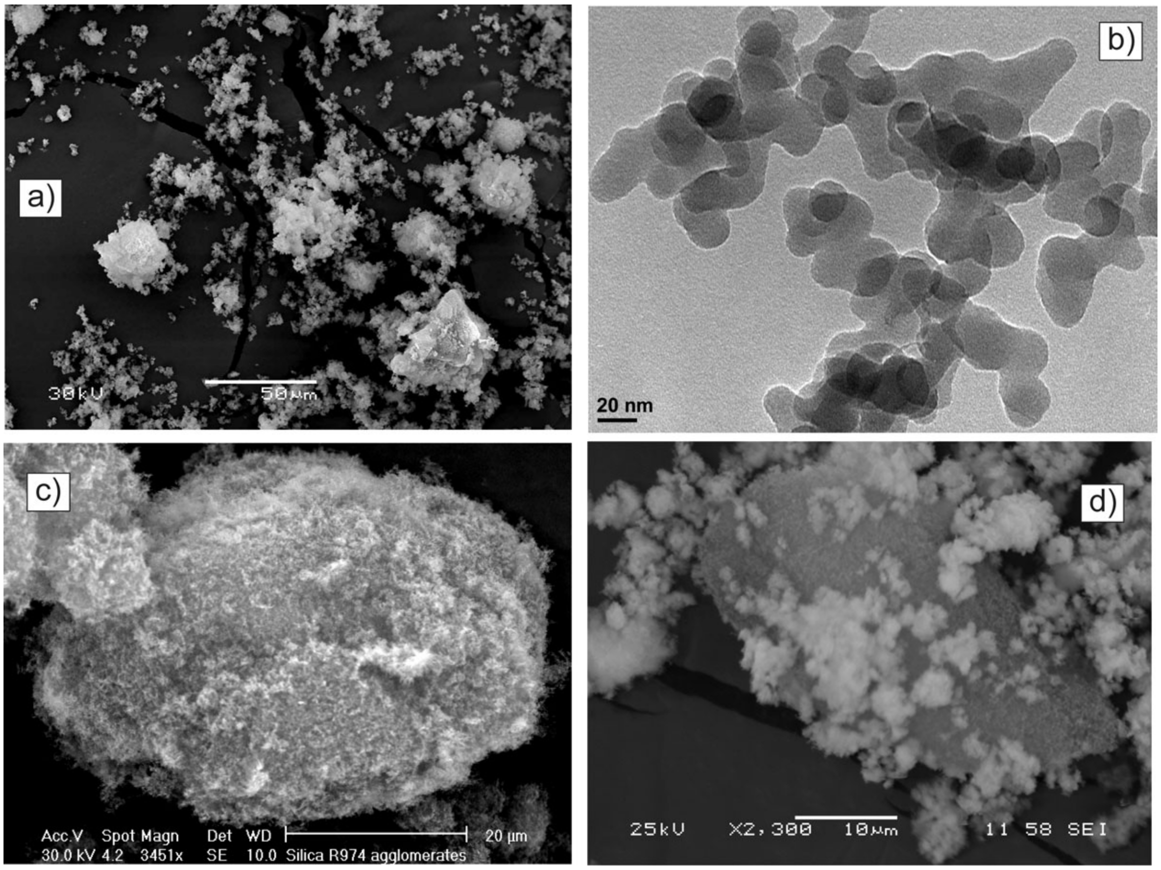

Figure 1. (a) SEM picture of the $Ca(OH)_2$ powder (as received) used in this work.

(b) TEM picture of nano-silica aggregates as formed due to particle sintering (c) SEM picture of a nano-silica agglomerate. (d) SEM picture of a nano-silica agglomerate coated with $Ca(OH)_2$ particles in the $Ca(OH)_2$/nano-silica composite. Images (a), (c) and (d) were taken using a JEOL 6460LV microscope. Image (b) was taken using a Philips CM200 TEM microscope.

modified one ($Ca(OH)_2$/nano-silica composite with 15% by weight of nano-silica) will be investigated.

As our goal is to investigate the mechanical strength of the adsorbents after calcination, raw samples were preheated in an oven up to 850°C at a rate of 6°C/min and kept at 850°C for 45 min. SEM micrographs of the calcined samples are shown in Figure 2. Figures 2b, 2c show material sintering at the contact between nano-silica and CaO, which gives rise to the formation of calcium silicates as can be seen in the XRD pattern obtained for the calcined CaO/nano-silica composite (Figure 2d).

Pore size distributions for raw and calcined samples of the original and modified adsorbents are shown in Figure 3a (obtained by means of a TriStar II 3020 V1.03 physisorption analyzer operated by N_2 sorption at 77 K). Figure 3b shows typical tiny crystals on the surface of raw $Ca(OH)_2$. The morphology of the $Ca(OH)_2$ particles' surface is changed after dehydration and sintering caused by calcination. Figure 3c shows dendritic like structures developed after calcination with a typical length larger than the crystals seen in the raw sample. As a consequence, the pore size distribution is shifted to larger pore sizes (Figure 3a). The pore distribution of the modified adsorbent is less distorted, which indicates a higher thermal stability as seen in the SEM images of raw and calcined samples shown in Figures 3d, e. This can be also inferred from measurements of the BET surface area, which decreased from 16.3 m^2/g for the fresh original adsorbent to 13 m^2/g after calcination whereas it decreased from 40 to 37.7 m^2/g after calcination for the modified adsorbent. As will be seen, material sintering and reaction between nano-silica and CaO during calcination will also have an effect on the mechanical stability of the adsorbent.

After being calcined, the powders were sieved using a sieve with 710 μm nominal opening size (ISO 3310-1). The PSDs of the sieved samples were obtained by means of a Mastersizer 2000 (Malvern Instruments). This instrument measures particle size by laser diffractometry of a predispersed sample according to the international standard for laser diffraction measurements ISO13320-1. Laser diffractometry is based on the principle that particles passing through a laser beam will scatter light at an angle that is directly related to their size. The diameter of the sphere that yields an equivalent light scattering pattern to the particle being measured corresponds approximately to the sphere of equivalent average cross-sectional area. As laser diffraction is a volume-based technique, the dynamic range covered is quite broad (between 0.02 and 2000 μm), allowing for the detection of well-dispersed particles as well as, in the case of fine cohesive powders, big aggregates.[26] Dispersion of the aggregates may be achieved either by air or a liquid. Air dispersion is performed using a Scirocco 2000 dry accessory (Figure 4). In this dispersion unit, the dry powder sample is placed in a vibrated tray and falls into the main feed mechanism, whose entrance is a wire sieve filled with ball

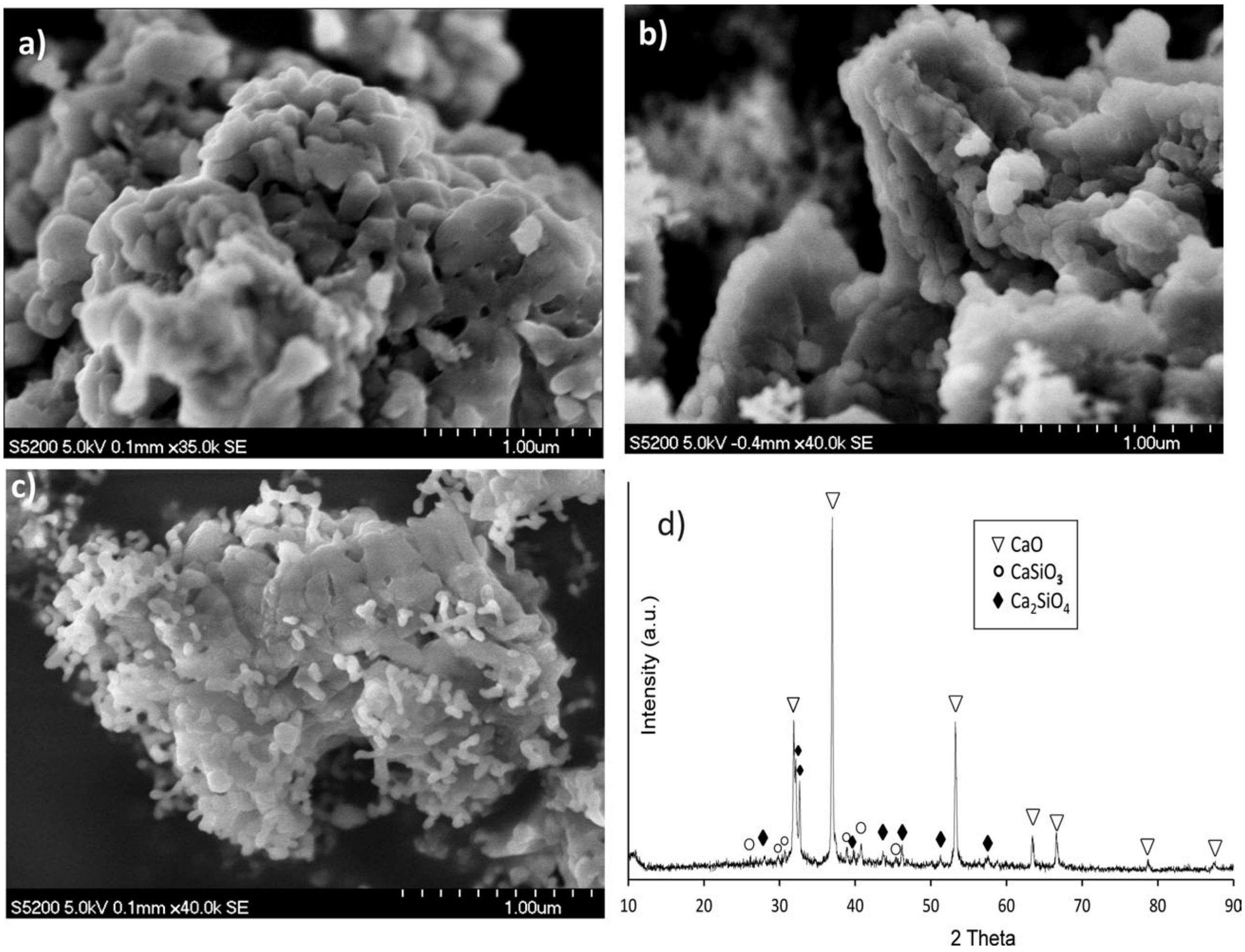

Figure 2. (a) SEM picture of CaO after Ca(OH)$_2$ calcination.

(b) and (c) SEM pictures of the CaO/nano-silica composite after calcination. (d) XRD pattern of a calcined CaO/nano-silica composite. Images (a), (b) and (c) were taken using a HITACHI Ultra High-Resolution S-5200 microscope. The XRD pattern was obtained by means of a Bruker D8 Advance powder diffractometer equipped with a high temperature chamber.

bearings. The ball bearings smooth the flow of the sample and also help to break up loose agglomerates. As the sample falls through the sieve it is accelerated by compressed air within a venturi against and around a bend as schematized in Figure 4, which helps to further break the agglomerates. Then, the sample changes direction and goes out from the dispersion unit, sliding on the wall of a tube in a spiral motion until it finally arrives at the measuring cell. According to the International Standard for particle size analysis using Laser Diffraction methods (ISO 13320), all the particles should ideally have the same approximate velocity in the measurement zone to avoid velocity bias in the results. Control of the air dispersive pressure is provided over a range between 0.1 and 3 bar, which generates air jet velocities between ~ 10 and ~ 70 m/s.[15] For aggregated particles, the shear stresses generated by these high velocities, as well as mechanical collisions in the case of strong aggregates, should break the aggregates. Usually, strongly cohesive aggregates cannot be fully dispersed at low pressures. Consequently, the amount of fine particles is observed to increase upon increasing the dispersive air pressure as the efficiency of dispersion is improved.[27] Calvert et al. have correlated the dispersion efficiency in the Scirocco unit to the bulk powder cohesiveness as measured by a Schulze ring shear tester.[27] A good dispersion is achieved if the size distribution remains nearly constant with increasing pressure. Dry powders can be also dispersed in a liquid (ISO 14887). Wetting particles' surface by the dispersant molecules of the liquid decreases their surface energy, thus reducing interparticle contact forces, which would serve to create a suspension of individual particles. The wet sample dispersion unit used in our work is the Hydro 2000S, which comprises an electric motor that drives a stirrer and impeller in the dispersion tank to provide a simultaneous stirring and pumping action that moves the agitated sample to the cell located in the optical bench via the sample tubing. In the case of strongly bound agglomerates, liquid dispersion can be further assisted by high energy ultrasonic irradiation. Ideally, the PSDs obtained from proper dry and liquid dispersion should be similar. However, fragmentation of low strength materials may occur from high energy collisions during dry dispersion, which would yield a particle size reduction. High energy ultrasonication in liquid dispersion might also cause particles attrition to a great extent by their interaction with collapsing cavities in the liquid.[28] If the powders have followed a pretreatment, or have been prepared, involving high temperatures, primary particles may be held together by strong chemical bonds due to material sintering,[18] thus forming strong compact aggregates that can be considered as effective porous particles.

In our work, we investigated the mechanical strength of calcined samples of the Ca-based adsorbents above described from the PSDs obtained by both dry and liquid dispersion.

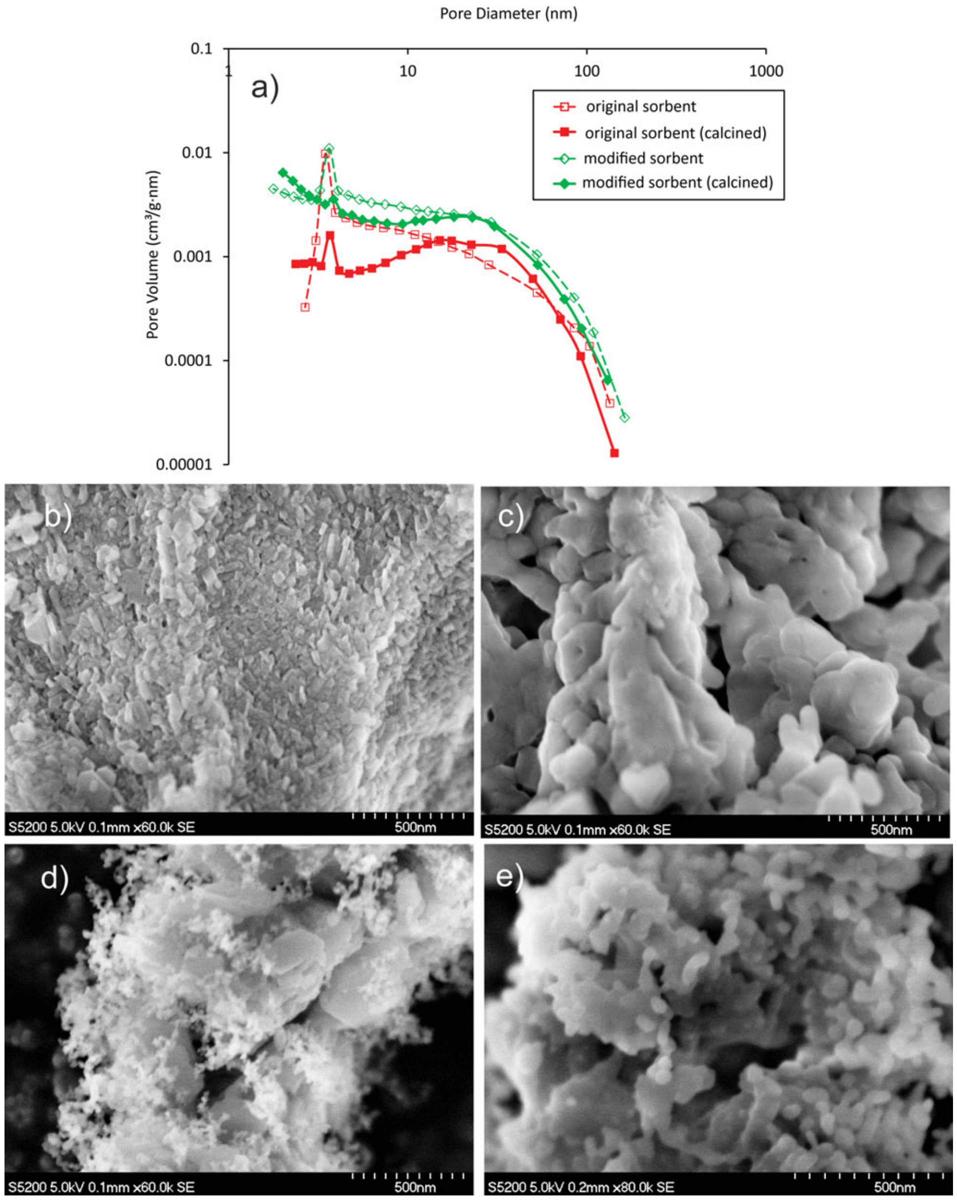

Figure 3. (a) BJH desorption (dV/dD) pore volume distributions for the (a) original ($Ca(OH)_2$) and (b) modified ($Ca(OH)_2$/nano-silica composite) adsorbents before and after calcination at 850°C.

(b) SEM picture of fresh $Ca(OH)_2$. (c) SEM picture of calcined CaO. (d) SEM picture of fresh $Ca(OH)_2$/nano-silica composite. (e) SEM picture of calcined CaO/nano-silica composite.

The PSDs of dry dispersed samples were obtained in the range of pressures from 0.1 to 3 bars. In liquid dispersion, 2.5 g of presieved sample was added to 100 ml of 2-propanol (as recommended for Ca-based materials according to ISO 14887). The effect of pre-ultrasonication was also studied by subjecting the liquid suspension to high energy ultrasonic irradiation (150 W, 40 kHz) for 10 min before taking it to the liquid dispersion unit.

Experimental results

In Figure 5, we show the PSDs obtained from raw $Ca(OH)_2$ and calcined CaO obtained by wet dispersion (ultrasonication assisted) to look for primary particle size. Note that calcination gives rise to a slightly different PSD when compared to the PSD of fresh $Ca(OH)_2$. Even though the average primary particle size is around 3 μm in both cases, a remarkably larger population of large particles (of size larger than 10 μm) and a smaller population of fine particles (of size smaller than 1 μm) is observed in the PSD of fresh $Ca(OH)_2$. This result suggests that ultrasonication causes the breaking of calcined particles as due to a lower mechanical strength.

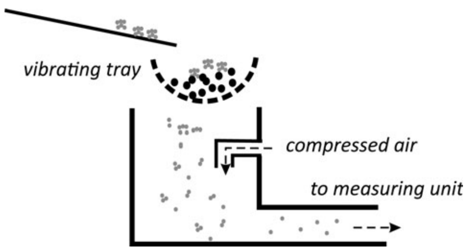

Figure 4. Sketch of the dry dispersion unit to measure particle size by laser diffractometry.

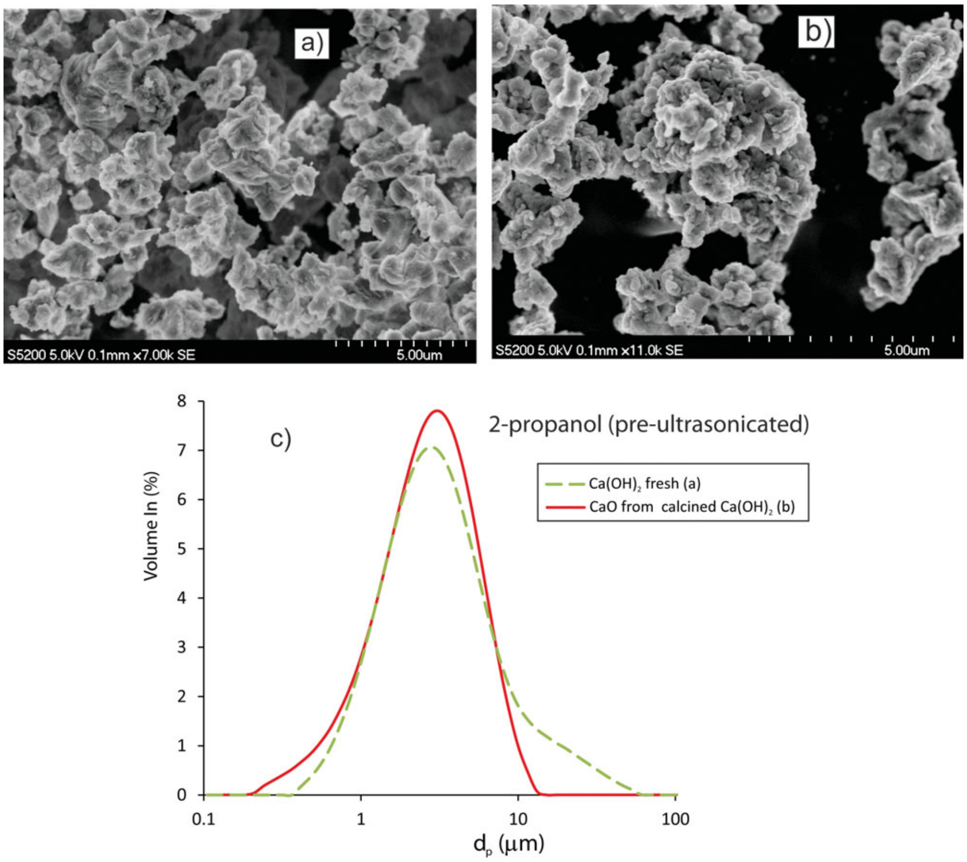

Figure 5. SEM pictures of $Ca(OH)_2$ (a) and CaO obtained from $Ca(OH)_2$ calcination (b).

To obtain these SEM images the samples were predispersed by a high pressure gas jet on the slide of a HITACHI Ultra High-Resolution S-5200 microscope. (c) PSDs obtained by dispersing the samples in 2-propanol with previous ultrasonication. [Color figure can be viewed in the online issue, which is available at wileyonlinelibrary.com.]

PSDs (volume distributions) of dry dispersed samples using the lowest dispersive pressure ($p_0 = 0.1$ bar) are plotted in Figure 6. As can be seen, the distribution of calcined CaO shows three well differentiated peaks at sizes $d_2 \simeq 417$ μm, $d_1 \simeq 25$ μm, and $d_0 \simeq 3\mu$m. The population centered around d_1 would indicate the presence of CaO aggregates corresponding to the relatively small $Ca(OH)_2$ aggregates observed in SEM images of the fresh sample (Figure 1). Material sintering at interparticle contacts within these aggregates during calcination would give rise to strong bonds between the particles. Due to the high cohesiveness of CaO, large aggregates (with a size even larger than the sieve opening size) are seen to be formed after sieving because of attractive van der Waals forces between the small aggregates. The population centered around $d_2 \simeq 417$ would correspond to the presence of these large, loose aggregates formed by van der Waals attractive forces after calcination. Their significant population for calcined CaO at small dispersive pressures indicate that many of them could not be broken by the $\sim$ 10 m/s air jet. In the case of the calcined CaO/nano-silica composite, the population of these relatively large aggregates is not remarkable. Moreover, this population is centered around a smaller size ($d_2 \simeq 275$ μm) compared to calcined CaO. This reveals the effectiveness of nano-silica in improving the powder flowability by reducing van der Waals attractive forces and thus avoiding the formation of large aggregates. Finally, the PSDs exhibit a small population of particles centered around a size $d_0 \simeq 3$ μm. As seen in SEM images and PSDs of the pre-ultrasonicated powders (Figure 5), this value is around the average size of the primary particles of CaO.

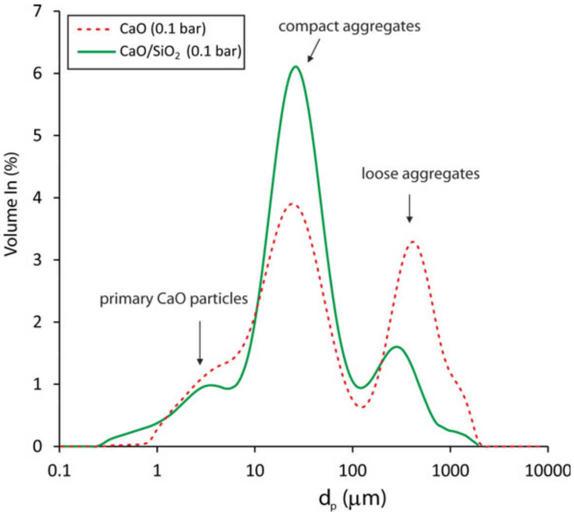

Figure 6. Particle size volume distributions of calcined CaO and calcined CaO/nano-silica composite measured for the minimum value of the dispersive air pressure (0.1 bar).

[Color figure can be viewed in the online issue, which is available at wileyonlinelibrary.com.]

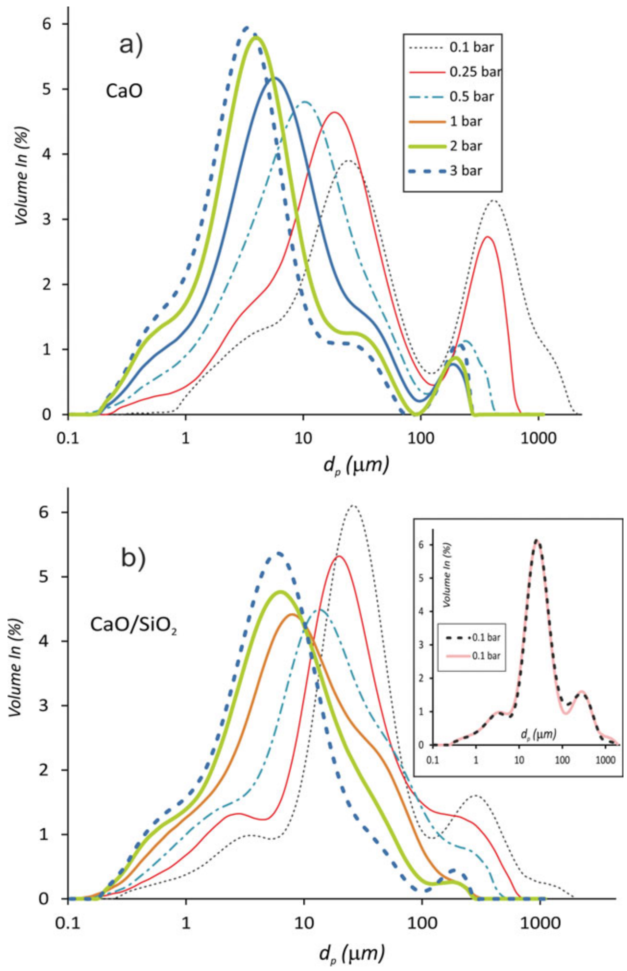

Figure 7. Particle size volume distributions of samples of calcined CaO and calcined CaO/nano-silica composite as affected by the dispersive air pressure.

The inset of (b) shows the results for different samples of the same adsorbent in order to demonstrate reproducibility of the data. [Color figure can be viewed in the online issue, which is available at wileyonlinelibrary.com.]

The PSDs obtained as the dispersive air pressure p_0 is increased are plotted in Figure 7. A main feature is that d_1 and d_2 are decreased as p_0 is increased, as might be expected due to the breaking of both large and small aggregates. In the case of calcined CaO, the marked decrease of the population of the large aggregates indicates their low resistance to mechanical stresses, as might be expected since they are formed by van der Waals attractive forces. As these loose large aggregates are broken into small compact aggregates, the population of large aggregates decreases while the population of small compact aggregates is increased. The size of the small compact aggregates d_1 decreases steadily as the dispersive air pressure is increased, indicating that the collisions produced by the high velocity air jet have sufficient energy to break sintered CaO contacts. At the largest pressure ($p_0 = 3$ bar), d_1 is decreased down to a value similar to the primary particle size. In the case of the CaO/nano-silica composite, since the population of large loose aggregates is small, the main effect of jet air dispersion is only to break the small compact aggregates. In contrast with the case of calcined CaO, their population decreases as the dispersive pressure is increased since the number of small compact aggregates generated by the breaking of the small population of large, loose aggregates is not significant. Note, however, that the trend in the population of small compact aggregates is reversed when the dispersive pressure is increased above 0.5 bar. At higher pressures, the height of the peak is increased with the dispersive air pressure, which suggests that the aggregates broken above 0.5 bar have a size larger than d_1 for the most part. Moreover, the value of d_1 does not decrease further when the dispersive air pressure is increased above 2 bar and reaches a constant value around $d_1 \simeq 6$ μm, indicating that in the case of the calcined CaO/nano-silica composite, even the highest dispersive air pressure (producing air jet velocities of about 70 m/s) cannot break small aggregates into primary particles.

Figure 8a shows d_1 as a function of the dispersive air pressure p_0 for calcined samples of CaO and CaO/nano-silica composite. As can be observed, d_1 decreases at a lower rate with p_0 for the calcined CaO/nano-silica composite when compared to the case of calcined CaO. Figures 8b–d show values of average particle sizes as calculated from different statistical analysis. As seen in Figure 9b, the evolution of the volume median diameter with the dispersive air pressure can be fitted to a power law $\langle d_\mathrm{p} \rangle = \alpha p_0^\beta$, where β would indicate the rate of reduction of the average aggregate size with the dispersive air pressure. According to the experimental data, it is $\beta = -0.72$ for CaO and $\beta = -0.51$ for the CaO/nano-silica composite. Likewise, the decrease of the surface weighted mean $D[3,2]$ and volume weighted mean $D[4,3]$ with p_0 is lessened for the CaO/nano-silica composite, further indicating the higher mechanical strength of the modified adsorbent.

PSDs of calcined CaO and CaO/nano-silica samples obtained using the wet dispersion unit, along with the PSDs of the samples dispersed by high velocity air jet at the minimum and maximum dispersive pressures ($p_0 = 0.1$ and 3 bar), are compared in Figure 9. Let us first analyze in detail the PSDs of calcined CaO. As can be observed, the PSD of the ultrasonicated sample exhibits a well-defined peak centered around a size d_1^*, which is similar to the value obtained using dry dispersion at 3 bar [$d_0^* \simeq d_0$ (3 bar) $\simeq 3$ μm] and would correspond to the average size of primary CaO particles. Even though calcination might have yielded sinterization of contacts within the compact aggregates, these aggregates are broken by ultrasonication and for the most part also by the highest velocity air jet in dry dispersion. Conversely, the PSDs of calcined CaO/nano-silica obtained by wet dispersion show a qualitatively distinct feature. These distributions appear to be bimodal. The PSD of pre-ultrasonicated calcined CaO/nano-silica exhibits a well-defined peak also centered around the value $d_0^* \simeq 3$ μm, which might likely be due to the breaking of compact aggregates of CaO particles that were not mixed with the nano-silica and to the erosion of primary CaO particles from the composite aggregates. Nevertheless, the other peak is centered around a value d_1^*, which is similar to the value of the peak obtained for the PSD of the air-dispersed sample at the lowest dispersive air pressure [$d_1^* \simeq 25$ μm $\simeq d_1$ (0.1 bar)], which suggests that ultrasonication is not capable of breaking the CaO/nano-silica composite aggregates. This result is reminiscent of the use of nano-silica as additive in high performance cement-based materials, which has been shown to enhance their compressive strength and abrasion resistance.[29]

Discussion

In accordance with the PSDs obtained and SEM observations described in the previous section, let us consider the

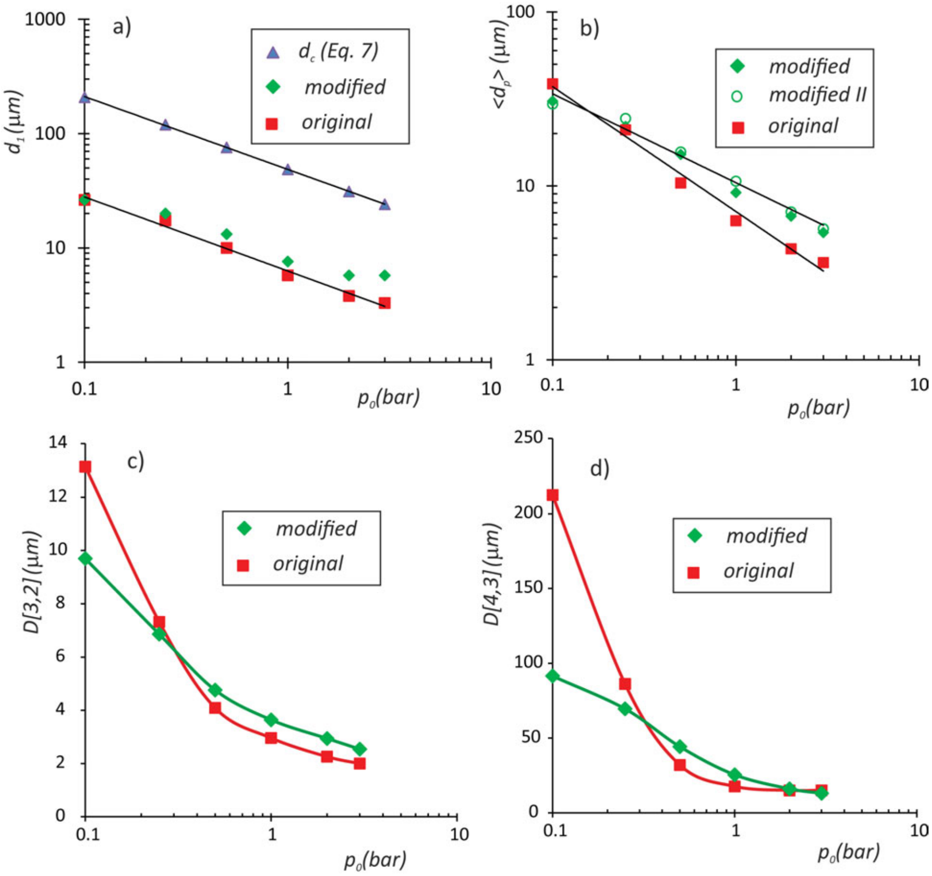

Figure 8. Evolution of effective particle sizes of the modified and original adsorbents as a function of the dispersive air pressure.

(a) d_1: size at the peak of the PSDs for the population of small compact aggregates. The solid line is a power law fit to the data for calcined CaO ($d_1 = 6.283p_0^{-0.648}$). The critical particle size for fragmentation d_c calculated from Eq. 7 ($d_c = 48.59p_0^{-0.637}$) is also plotted. (b) Volume median diameter. Solid lines are best power law fits to the data ($\langle d_p \rangle = 7.12p_0^{-0.717}$ for the original adsorbent and $\langle d_p \rangle = 10.424p_0^{-0.511}$ for the modified adsorbent). (c) Surface area moment mean diameter (Sauter mean). (d) Volume moment mean diameter (De Brouckere mean). Results obtained for different samples of the same adsorbent are shown in (b) to demonstrate reproducibility of the data. [Color figure can be viewed in the online issue, which is available at wileyonlinelibrary.com.]

compact, small aggregates in the calcined samples as effective porous particles of size d_1, wherein contacts between primary particles are sintered during calcination and which can aggregate further due to van der Waals forces to form large, low strength aggregates. The results show that, besides of the effect of nano-silica in decreasing van der Waals force of attraction, which reduces the formation of large loose aggregates, an additional benefit of the use of this additive is that the composite aggregates of the modified sorbent exhibit a relatively higher mechanical strength when compared to the compact aggregates of calcined CaO. In this section, we will analyze the results inferred from the PSDs on the breaking of these compact aggregates due to mechanical collisions generated in the dry dispersion unit.

According to single particle impact tests,[6] the type of fracture mechanism of calcined CaO due to collisions against a target is strongly dependent on the nature of the material, on its preprocessing, and on its impact velocity. Fragmentation of raw limestone in impact tests is significant in the range of impact particle velocities v_p between 10 and 45 m/s, which fits the typical values of gas jet velocities in practical applications.[6] Using a mechanistic model to analyze the impact attrition of particles by impact against a target, Ghadiri and Zhang[30] proposed the equation $f \propto \rho\, v_p^2 d_p H/K_c^2$ to account for the fractional loss of material (f) due to semi-brittle fracture. Here, the relevant material properties included are particle density ρ, characteristic particle size d_p, material hardness H, and material fracture toughness K_c. The trends of the experimental results on single particle impact tests agreed with the predictions of this model for ionic crystals (MgO, NaCl, and KCl),[31] as well as for catalyst particles.[14] According to SEM images of the debris of ionic crystals particles after impact, the inferred primary mechanism of attrition was chipping.[31] Material removal was observed to mainly occur from the corners and edges of the particles by the propagation of subsurface lateral cracks, leading to the generation of a limited number of fragments of a size much smaller than the parent particle size. In the case of catalyst particles, the debris consisted mainly of burrs and micro-spheroids that fractured from the agglomerate.[14] In attrition caused by air-jets, there is a strong effect of the structure of the jet on the breakage mechanism.[13,14] As seen for catalyst particles, the impact mechanism predominates when the size of the orifice is larger than particle size.[13,14]

The PSDs obtained by Scala et al.[6] suggested that fragmentation of raw limestone also took place by chipping at impact velocities smaller than 25 m/s but that splitting was the dominant mechanism at higher impact velocities, that is,

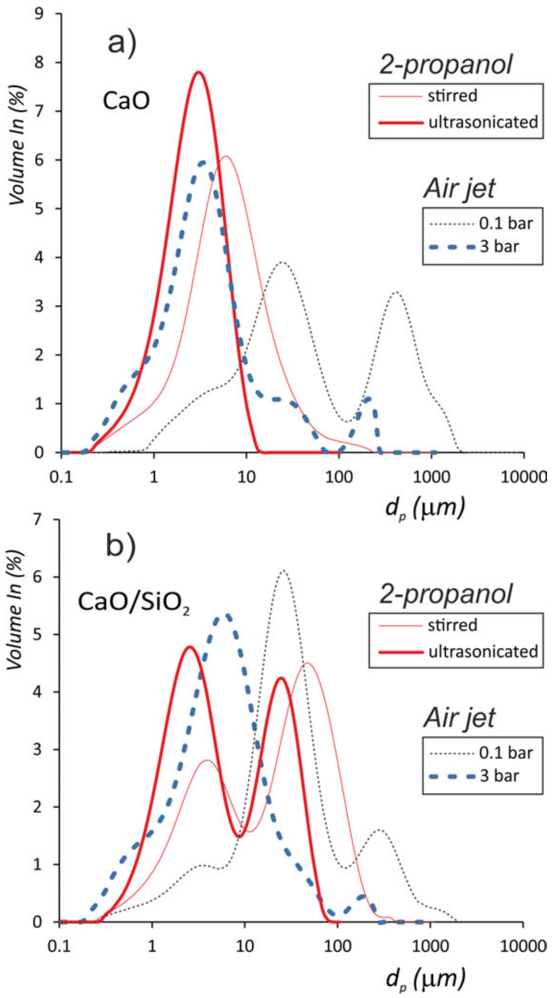

Figure 9. Particle size volume distributions of calcined samples of the original ($Ca(OH)_2$) and the modified ($Ca(OH)_2$/nano-silica composite) adsorbents for dispersive air pressures of 0.1 bar and 3 bar, and PSD of a calcined sample of the original adsorbent dispersed in propanol by stirring it using a wet dispersion unit.

The PSD of a sample dispersed using the wet dispersion unit and previously subjecting it to ultrasonic fragmentation is also shown. [Color figure can be viewed in the online issue, which is available at wileyonlinelibrary.com.]

particles broke into a relatively small number of fragments of a size comparable with the parent particle size. On the contrary, the PSDs obtained for calcined and recarbonated limestones were indicative of the generation of a large number of small fragments by an extensive loss of particle connectivity.[6] Previously reported impact tests suggested that the transition between chipping and fragmentation failure modes occurred on calcined and sulphated limestones at impact velocities above 10 m/s.[5] At higher impact velocities, according to SEM images, the cracks due to impact did no longer curve out towards the particles' surface but crossed the particles, causing their splitting into relatively large fragments.[5]

Unfortunately, the current setup of the laser diffractometer apparatus used in our experiments does not allow for the recovery of the material for SEM analysis to have an idea of the type of fragmentation mechanism. Nonetheless, this information may also be indirectly inferred from a careful analysis of the evolution of the PSDs (Figure 7). Accordingly, the PSDs obtained as the dispersive air pressure is increased suggest that splitting of the compact aggregates is the main fracture mechanism. Otherwise, a marked separate population of primary particles should appear due to erosion of the compact aggregates.

Using Weibull's statistical analysis on the fragmentation mechanics of brittle materials,[32] Yashima et al. obtained the fracture stress causing splitting fragmentation of nearly perfect spherical specimens under slow-rate compression due to the presence of minute flaws or cracks in the material.[33,34] Since flaws or cracks can vary substantially in size, shape, and type, large variations in strength are expressed in terms of a failure probability, which is a power-law function of the stress. The strength of a given particle is thus determined by the weakest crack and depends on the particle volume. Assuming that cracks are randomly distributed and that there is a constant density per unit volume, the number of cracks increases as the particles size increases. The energy required to fracture a particle of size d_p can be expressed by the equation $E_0 = Cd_p^{(3m-5)/m}$, where m is Weibull's coefficient of uniformity and C is a constant depending on the Young modulus and Poisson's ratio of the material.[33,34] Assuming that the kinetic energy of a particle that collides with a grinding medium is completely converted into fracture energy causing fragmentation, as in their experimental study on crushing of single spheres, Yashima et al.[33] obtained that the impact velocity required for fracturing a particle can be related to its size according to the equation

$$v_p = Kd_p^{-5/2m} \tag{1}$$

where K is a constant depending on material properties. The variation of the impact velocity with particle size is influenced significantly by the values of m. From their experimental results in crushing tests, Yashima and coworkers[33,34] found that Weibull's coefficient varied from 2.6 to 24.9 depending on the type of material.[33] In general, the values of m are low for soft materials but tend to be high for hard materials. Large coefficients indicate a weaker particle-size dependence of the fracture energy. Thus, the effect of particle size decreases with increasing the value of m, which tends toward infinity for ideal materials. The Weibull coefficient reported for limestone was $m = 3.2$ and for glass (borosilicate glass and quartz glass), which is a harder material, was $m = 5.93$.

As in our experiment, the randomly distributed interparticle contacts within compact aggregates might be expected to have different levels of strength due to degree of material sintering at contacts, the use of the above theory to describe their fragmentation seems to be justified. Nevertheless, a correlation must first be found between the air jet velocity and the actual particles' velocity at impact in the Scirocco dry dispersion unit used in our experiment. Note that the geometry of the dispersion unit differs from that of a fluidized bed where attrition occurs due to the entrainment of the particles in air jets ejected from perforated orifices at the gas distributor plate. As schematically represented in Figure 4, a diluted cloud of aggregates falls in the dispersion unit into the region of the downwards pointing air jet. These aggregates are then accelerated up to a velocity that would be determined by the air velocity, the system geometry and the collisions between aggregates. Let us assume that aggregates can be considered as individual spherical particles of mass m_p.

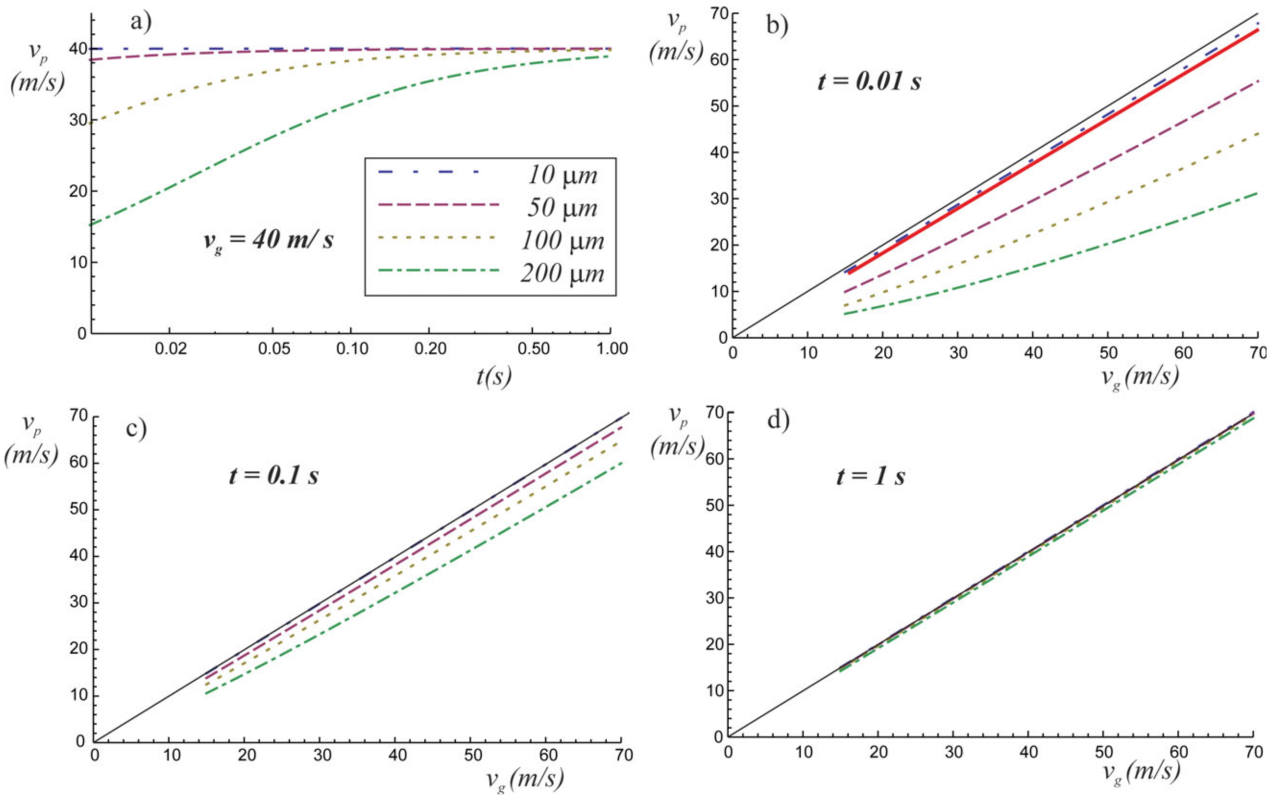

Figure 10. (a) Velocity of a particle v_p in a gas stream (gas velocity v_g = 40 m/s) as a function of time for different values of particle size (indicated).

(b) v_p as a function of v_g at $t = 0.01$ s. (c) v_p as a function of v_g at $t = 0.1$ s. (d) v_p as a function of v_g at $t = 1$ s. The solid line in b, c, and d indicates $v_p = v_g$. Physical parameters used for the calculations are particle density $\rho_p = 2360$ kg/m^3, gas viscosity $\eta = 1.8 \times 10^{-5}$, gas density $\rho_g = 1.25$ kg/m^3. The red thick line in (b) shows the curve obtained for a particle of size 25 μm and internal porosity 0.5. [Color figure can be viewed in the online issue, which is available at wileyonlinelibrary.com.]

The acceleration of a particle when it experiences the gas drag force caused by the air jet is governed by Newton's second law of motion

$$m_p \frac{dv_p}{dt} = F_D \tag{2}$$

where v_p is the particle's velocity and F_D is the gas drag force, which is given by

$$F_D = \frac{1}{2} c_D A_p \rho_g (v_g - v_p)^2 \tag{3}$$

where A_p is the cross-sectional area of the particle ρ_p is the particle density, ρ_g is the gas density, and c_D is the drag coefficient. In the case of spherical particles, it is $A_p = (1/4)\pi d_p^2$, $m_p = (1/6)\rho_p d_p^3$, and the drag coefficient can be approximated by the equation[35]

$$c_D \simeq \frac{24}{\mathrm{Re}_p} + \frac{6}{1+\sqrt{\mathrm{Re}_p}} + 0.4 \tag{4}$$

where Re_p is the particle's Reynolds number $\mathrm{Re}_p = \rho_g v_p d_p/\eta$, and η is the gas dynamic viscosity. Equation 4 is a valid approximation within an extended range of Reynold's number ($0 < \mathrm{Re}_p < 2 \times 10^5$).[35]

Examples curves of the particle's velocity obtained by numerically solving Eq. 2 assuming that the gas velocity v_g is constant are plotted in Figure 10. Figure 10a shows v_p as a function of time for a typical gas velocity $v_g = 40$ m/s and for different values of particle size. v_p is represented as a function of v_g at $t = 0.01$ s (Figure 10a), $t = 0.1$ s (Figure 10b), and $t = 1$ s (Figure 10c). As can be seen, the time for the particles to reach the gas velocity is a strong function of particle size. Particles smaller that 10 μm reach the gas velocity in less that a tenth of a second. The velocity of particles of size on the order of tens of microns equals the gas velocity in less than a second and particles with size of a few hundred of microns require about 1 s to attain the gas velocity. These times would be smaller if we take into account that the density of the aggregates is smaller than the particle density that has been used for the calculations. In Figure 10c, the curve corresponding to a porous particle (using a porosity of 0.5) of size $d_p = 25$ μm is plotted, showing that these effective particles reach the jet velocity in about one tenth of a second.

Assuming that attrition is mostly caused by impacts occurring after all of the aggregates have reached a velocity similar to the gas velocity ($v_p \sim v_g$) and using Eq. 1, it can be estimated that an aggregate with a size larger than a critical size $d_c \propto v_g^{-2m/5}$ will collide with sufficient kinetic energy for fracturing. The probability of an aggregate of having a size $d_p \geq d_c$ would be

$$P(x = d_p \geq d_c) = \int_{d_c}^{\infty} P_0(x)\,dx \leq \frac{1}{d_c}\int_{d_c}^{\infty} x P_0(x)\,dx \leq \frac{1}{d_c}\int_{0}^{\infty} x P_0(x)\,dx = \frac{\langle d_p \rangle_0}{d_c} \tag{5}$$

where $P_0(x)$ and $\langle d_p \rangle_0$ are the probability density function and average aggregate size before fragmentation, respectively. Equation 5 is usually known as Markov's inequality in mathematical statistics theory.[36] When an aggregate of the sample in our experiment collides with a velocity v_p, the probability that it is fragmented scales proportionally with its probability of having a size $d_p \geq d_c$. As v_g is increased, d_c is decreased, and thus a larger fraction of particles will be fragmented. From Markov's inequality, it is thus plausible that the fraction of fragmented particles scales as $f \propto 1/d_c \propto v_p^{2m/5}$. Using $m = 3.2$ (as reported for limestone from independent measurements by Yashima and co-workers[33,34]), we obtain $f \propto v_p^{1.28}$. Note that the exponent of this theoretical power law is a very similar value to the experimental exponent obtained for the fractional mass of fragments in impact tests on calcined limestone by Scala et al. ($k \simeq 1.3$),[6] which suggests that Eq. 1 might be useful to estimate the level of attrition suffered by Ca-based adsorbents due to impacts.

In our experiment, the gas jet velocity v_g and the dispersive air pressure p can be approximately related by the Darcy–Weisbach equation[37]

$$p_0 = A v_g^2 \tag{6}$$

where A is a constant depending on the pipe geometry and the density of the fluid. At $p_0 = 3$ bar, the air speed is $v_g \simeq 70$ m/s.[15] Thus, $A \simeq 6.1 \times 10^{-4}$ (bar s^2) m^2 (13 m/s $\lesssim v_g \lesssim$ 70 m/s in the range of dispersive pressure applied). Yashima et al.[33] calculated, using the theory described above, that a typical value of the impact velocity required to fracture a 100 μm sized limestone particle was 23 m/s,[33] which fits in the range of air jet velocities in the laser diffractometry measurements. Using $v_g = 23$ m/s, $d_p = 100$ μm, and $m = 3.2$ in Eq. 1, the value of the constant K for limestone can be estimated and, from Eqs. 1 and 6, the critical particle size for fragmentation would be

$$d_c = \left(\frac{p_0}{A K^2}\right)^{-m/5} \tag{7}$$

Equation 7 is plotted for limestone in Figure 8a along with experimental data on the size for compact small aggregates (d_1) inferred from the measured PSDs on dry dispersed samples of calcined CaO. As can be seen, d_1 scales proportionally to the predicted critical size for fragmentation. In the experiments reported by Yashima et al.,[33] the required impact velocity for fracturing relatively harder glass particles was larger than 100 m/s. It was 114 m/s for silica (quartz) and 225 m/s for borosilicate.[33] This would explain why in our experiments the addition of nano-silica makes the composite compact aggregates harder, which would serve to lessen their size reduction (Figure 8a).

Conclusion

Attrition tests have been reported for Ca-based adsorbents based on particle sizing by means of laser diffractometry. In this technique, the material is dispersed using a high velocity air jet capable of fragmenting the aggregates due to mechanical collisions. The PSDs obtained as a function of the dispersive air pressure serve to evaluate the resistance to attrition of the Ca-based adsorbent. From the PSD of calcined CaO at low dispersive pressures, two types of aggregates have been identified. Compact sintered aggregates, of size around 25 μm, form large loose aggregates due to attractive van der Waals forces that are rapidly broken as the dispersive air pressure is increased. The compact aggregates are progressively broken as the dispersive air pressure is increased down to primary particles at the highest air-jet velocities (of about 70 m/s). In the case of the modified adsorbent consisting of CaO/nano-silica composite, van der Waals forces are decreased and the population of large loose aggregates is remarkably diminished. The size of the relatively small, compact CaO/nano-silica aggregates decreases with the dispersive air pressure at a lower rate when compared to CaO, which can be explained by the hardening effect of nano-silica. This is confirmed by the PSDs obtained by dispersing pre-ultrasonicated samples in a liquid. Although ultrasonication could break the CaO aggregates down to the level of primary particle size, it was inefficient in breaking the Ca/nano-silica aggregates. From the evolution of the PSDs of dry dispersed calcined samples as the dispersive air pressure is increased, it is inferred that the attrition mechanism is mainly due to splitting of the sintered aggregates in a relatively small number of fragments of a size comparable to the parent aggregate size. Using Weibull's statistical analysis on the fracture mechanics of brittle materials, it is predicted that the average aggregate size decreases due to attrition proportionally to a critical size for particle fragmentation $d_c \propto v_0^{-2m/5}$, where $m \simeq 3.2$, which agrees with the experimental results obtained.

In this article, we studied the mechanical strength of adsorbents after calcination. It would be interesting, however, to test in a future work the mechanical strength of the adsorbents after many carbonation–calcination cycles. Nevertheless, it must be noted that experimental studies reported in the literature indicate that attrition in the Ca-looping process mostly occurs after first calcination.

Acknowledgments

This work was supported by the "Consejeria de Innovacion, Ciencia y Empresa (Junta de Andalucia)" within the European Regional Development Fund contracts FQM-5735 and by the Spanish Government Agency "Ministerio de Ciencia e Innovacion" (contract FIS2011-25161). The authors gratefully acknowledge the Microscopy, Functional Characterization, and X-ray services of the Innovation, Technology and Research Center of the University of Seville (CITIUS).

Literature Cited

1. Blamey J, Anthony EJ, Wang J, Fennell PS. The calcium looping cycle for large-scale CO2 capture. *Prog Energ Combust Sci*. 2010;36:260–279. doi:10.1016/j.pecs.2009.10.001.
2. Romano MC, Cassotti EN, Chiesa P, Meyerb J, Mastin J. Application of the sorption enhanced-steam reforming process in combined cycle-based power plants. *Energy Procedia*. 2011;4:1125–1132.
3. Arias B, Abanades JC, Grasa GS. An analysis of the effect of carbonation conditions on CaO deactivation curves. *Chem Eng J*. 2011;167:255–261. doi:10.1016/j.cej.2010.12.052.
4. Manovic V, Charland JP, Blamey J, Fennell PS, Lu DY, Anthony EJ. Influence of calcination conditions on carrying capacity of CaO-based sorbent in CO2 looping cycles. *Fuel* 2009;88:1893–1900. doi:10.1016/j.fuel.2009.04.012.
5. Scala F, Salatino P, Boerefijn R, Ghadiri M. Attrition of sorbents during fluidized bed calcination and sulphation. *Powder Technol*. 2000;107:153–167. doi:10.1016/S0032-5910(99)00185–0.
6. Scala F, Montagnaro F, Salatino P. Attrition of limestone by impact loading in fluidized beds. *Energy Fuels*. 2007;21:2566–2572.
7. Yao X, Zhang H, Yang H, Liu Q, Wang J, Yue G. An experimental study on the primary fragmentation and attrition of limestones in a fluidized bed. *Fuel Proces Technol*. 2010;91:1119–1124.
8. Gonzalez B, Alonso M, Abanades JC. Sorbent attrition in a carbonation/calcination pilot plant for capturing CO2 from flue gases. *Fuel* 2010;89:2918–2924. doi:10.1016/j.fuel.2010.01.019.

9. Coppola A, Montagnaro F, Salatino P, Scala F. Limestone attrition during fluidized bed calcium looping cycles for CO2 capture. In: Procedings of the 12th International Conference on Multiphase Flow in Industrial Plants (MFIP12). Italian Association Of Industrial Plant Engineering; 2011:IV7.
10. Manovic V, Anthony EJ. Long-term behavior of CaO-based pellets supported by calcium aluminate cements in a long series of CO2 capture cycles. *Ind Eng Chem Res*. 2009;48:8906–8912.
11. Pacciani R, Muller CR, Davidson JF, Dennis JS, Hayhurst AN. Synthetic Ca-based solid sorbents suitable for capturing CO2 in a fluidized bed. *Can J Chem Eng*. 2008;86:356–366.
12. Montagnaro F, Salatino P, Scala F, Urciuolo M. A population balance model on sorbent in CFB combustors: The influence of particle attrition. *Ind Eng Chem Res*. 2011;50:9704–9711.
13. Boerefijn R, Ghadiri M, Salatino P. *Attrition in fluidised beds*. In: Salman AD, Ghadiri M, Hounslow MJ, editors. *Particle Breakage*, vol. 12 of *Handbook of Powder Technology*. The Netherlands: Elsevier Science B.V., 2007:1019–1053.
14. Boerefijn R, Gudde N, Ghadiri M. A review of attrition of fluid cracking catalyst particles. *Adv Powder Technol*. 2000;11:145–174.
15. Ecker F, Mueller N, Nikolai D. Comparative studies of various methods for determining the friability of granules and the development of a quick test by laser diffraction. In: *DPhG Jahrestagung*. September 29th–October 1st, Jena, Germany; 2009.
16. Mueller N, Ecker F. Determining granule breaking strength by laser diffraction method. *Pharm Ind*. 2011;73:2061–2070.
17. Valverde JM, Pontiga F, Soria-Hoyo C, Quintanilla MAS, Moreno H, Duran FJ, Espin MJ. Improving the gas solids contact efficiency in a fluidized bed of CO2 adsorbent fine particles. *Phys Chem Chem Phys*. 2011;13:14906–14909. doi:10.1039/c1cp21939a.
18. Hyeon-Lee J, Beaucage G, Pratsinis SE, Vemury S. Fractal analysis of flame-synthesized nanostructured silica and titania powders using small-angle x-ray scattering. *Langmuir*. 1998;14:5751–5756.
19. Quintanilla MAS, Valverde JM, Espin MJ. Electrofluidization of silica nanoparticle agglomerates. *Ind Eng Chem Res*. 2012;51:531–538. doi:10.1021/ie200538v.
20. Yang J, Sliva A, Banerjee A, Dave RN, Pfeffer R. Dry particle coating for improving the flowability of cohesive powders. *Powder Technol* 2005;158:21–33. doi:10.1016/j.powtec.2005.04.032.
21. Qian Z, Wang P, Gogos CG. A novel method for preparing nanoparticle-coated additives used in polypropylene composites. *Polym Eng Sci*. 2012;52:1195–1205.
22. Gallo CF, Lama WL. Some charge exchange phenomena explained by a classical model of the work function. *J Electrostat*. 1976;2:145–150. doi:10.1016/0304-3886(76)90005-X.
23. Lide DR, editor. *CRC Handbook of Chemistry and Physics*, 88th ed.. Boca Raton, FL: CRC Press, 2007.
24. Valverde J, Duran F, Pontiga F, Moreno H. Co2 capture enhancement in a fluidized bed of a modified geldart c powder. *Powder Technol*. 2012;224:247–252. doi:10.1016/j.powtec.2012.02.060.
25. Valverde JM, Perejon A, Perez-Maqueda L. Enhancement of fast CO_2 capture by a nano-SiO_2/CaO composite at ca-looping conditions. *Environ Sci Technol*. 2012;46:6401–6408. doi:10.1021/es3002426.
26. Instruments M. Detecting oversized particles in ceramic powders using the mastersizer 2000. Application Note; Malvern Instruments; 2005.
27. Calvert G, Dyson M, Kippax P, Tweedie R, Ghadiri M. Aerodynamic dispersion of cohesive powders: an evaluation of disperser performance. Eds. Meesters G, Schmidt-Ott A, Vercoulen PHW, Laarhoven B van. In: *World Congress of Particle Technology 6*, Nürnberg, Germany: NürnbergMesse GmbH, 2010.
28. Kusters KA, Pratsinis SE, Thoma SG, Smith DM. Ultrasonic fragmentation of agglomerate powders. *Chem Eng Sci*. 1993;48:4119–4127. doi:10.1016/0009-2509(93)80258-R.
29. Sobolev K, Flores I, Torres-Martinez LM, Valdez P, Zarazua E, Cuellar EL. *Engineering of SiO_2 nanoparticles for optimal performance in nano cement-based materials*. In: Nemecek J, Bittnar Z, Bartos PJM, Bittnar Z, Bartos PJM, Smilauer V, Zeman J, editors. *Nanotechnology in Construction 3*. Berlin - Heidelberg, Germany: Springer, 2009:139–148.
30. Ghadiri M, Zhang Z. Impact attrition of particulate solids. part 1: a theoretical model of chipping. *Chem Eng Sci*. 2002;57:3659–3669.
31. Zhang Z, Ghadiri M. Impact attrition of particulate solids. part 2: Experimental work. *Chem Eng Sci*. 2002;57:3671–3686.
32. Amaral PM, Fernandes JC, Rosa LG. Weibull statistical analysis of granite bending strength. *Rock Mech Rock Eng*. 2008;41:917–928.
33. Yashima S, Kanda Y, Sano S. Relationships between particle size and fracture energy or impact velocity required to fracture as estimated from single particle crushing. *Powder Technol*. 1987;51:277–282.
34. Kanda Y, Sano S, Yashima S. A consideration of grinding limit based on fracture mechanics. *Powder Technol*. 1986;48:263–267.
35. White FM. *Viscous Fluid Flow*. New York: McGraw-Hill, 1974.
36. Grimmett G, Stirzaker D. Probability and Random Processes, 3rd ed. New York: Oxford, 2001. ISBN 0-19-857222-0.
37. Nevers ND. Fluid Mechanics for Chemical Engineers. Series 3^{rd}. New York: McGraw-Hill Chemical, 2004.

Manuscript received Mar. 12, 2012, and revision received Jun. 7, 2012.